Endmember Bundle Extraction Based on Multiobjective Optimization

Rong Liu, *Member, IEEE* and Xiaoxiang Zhu, *Senior Member, IEEE*

***Abstract*— A number of endmember extraction methods have been developed to identify pure pixels in hyperspectral images (HSIs). The majority of them use only one spectrum to represent one kind of material, which ignores the spectral variability problem that particularly characterizes a HSI with high spatial resolution. Only a few algorithms have been developed to identify multiple endmembers representing the spectral variability within each class, called endmember bundle extraction (EBE). This article introduces multiobjective particle swarm optimization for the identification of multiple endmember spectra with variability. Unlike existing convex geometry-based EBE methods, which operate on a single geometry of the dataspace, the proposed method divides the observed data into subsets along the spectral dimension and simultaneously operates on multiple dataspaces to obtain candidate endmembers based on multiobjective particle swarm optimization. The candidate endmembers are then refined by spatial post-processing and sequential forward floating selection to produce the final result. Experiments are conducted on both synthetic and real hyperspectral data to demonstrate the effectiveness of the proposed method in comparison with several state-of-the-art methods.**

***Index Terms*— Endmember bundle extraction (EBE), hyperspectral, multiobjective optimization, spectral variability.**

I. Introduction

With the ability to record abundant spectral information about materials, hyperspectral imagery has been widely used for various applications, including vegetation mapping [1], mineral exploration [2], agricultural assessment [3], and many others [4]–[6]. Hyperspectral unmixing (HU), currently a hot topic in the processing of hyperspectral images (HSIs), involves estimating quantitative abundances of pure ground components within a pixel, so as to derive quantitative information at the subpixel scale. The selection of pure ground components, referred to as endmembers, is important for the successful application of HU. Endmembers can be obtained either from observed data or from field or laboratory measurement. To reduce the amount of time and expense involved in field measurement and keep similar atmospheric effects between endmembers and the data to be unmixed, a number of methods have been proposed to automatically extract endmembers directly from the image data. Many of these approaches use a single spectrum to represent one kind of material and only extract a single endmember spectrum for each endmember class. Techniques in this category either directly extract endmembers from the image, for example, the pixel purity index (PPI) [7], N-FINDR [8], and vertex component analysis (VCA) [9], among many others [10]–[12], or they generate virtual endmembers without assuming the presence of pure signatures in the input data, such as minimum volume-based methods [13]–[15] and nonnegative matrix factorization-based methods [16]–[18]. The major drawback of these methods is that they ignore the endmember variability problem within each endmember class. However, the endmember variability problem is usually unavoidable in real HSIs [19]. For example, illumination differences in the scene can cause shape and magnitude variations within one endmember class. For a scene with large spectral variations, ignoring the endmember variability problem can lead to poor unmixing results.

Some solutions developed to solve the endmember variability problem incorporate multiple endmembers within each endmember class [20], [21]. Multiple endmember spectral mixture analysis (MESMA) [22], one of the most widely used and successful methods, selects an optimal endmember combination for each pixel from a spectral library that includes spectral variability. However, there is a heavy computation burden when there is a large number of candidate endmember combinations. To alleviate this problem, MESMA selects a small number of endmember spectra to represent spectral variability within the data instead of assessing all the available endmembers; however, this solution may lead to estimation error of the abundance fractions. More efficient unmixing methods to overcome endmember variability have been presented in the recent literature [19], [23]. Yet the premise of these unmixing methods is the availability of a spectral library that contains endmembers representing the spectral

Manuscript received June 25, 2020; revised October 19, 2020; accepted November 5, 2020. Date of publication November 24, 2020; date of current version September 27, 2021. This work was supported by the German Research Foundation (DFG) under Grant ZH 498/7-2. The work of Xiaoxiang Zhu was supported by the European Research Council (ERC) through the European Union's Horizon 2020 Research and Innovation Program under Grant ERC-2016-StG-714087, (Acronym: *So2Sat*), in part by the Helmholtz Association through the Framework of Helmholtz Artificial Intelligence Cooperation Unit (HAICU)-Local Unit "Munich Unit @Aeronautics, Space and Transport (MASTr)," in part by the Helmholtz Excellent Professorship "Data Science in Earth Observation-Big Data Fusion for Urban Research," and in part by the German Federal Ministry of Education and Research (BMBF) in the framework of the International Future artificial intelligence (AI) Laboratory "AI4EO–Artificial Intelligence for Earth Observation: Reasoning, Uncertainties, Ethics and Beyond." *(Corresponding author: Xiaoxiang Zhu).*

The authors are with German Aerospace Center (DLR), Remote Sensing Technology Institute (IMF), 82234 Weßling, Germany, and also with the Data Science in Earth Observation (former: Signal Processing in Earth Observation), Technical University of Munich (TUM), 80333 Munich, Germany (e-mail: rong.liu@dlr.de; xiaoxiang.zhu@dlr.de).

Digital Object Identifier 10.1109/TGRS.2020.3037249

variability within each endmember class. To date, there are only a few methods that can extract multiple endmembers with spectral variability, also called endmember bundles, from the image, indicating the need for new efficient endmember bundle extraction (EBE) methods.

The method developed in [24] divides the global image into spatial subsets and uses a traditional endmember extraction (EE) method such as N-FINDR to extract endmembers within each spatial subset, then integrates the endmembers of all the subsets to obtain the final multiple endmembers. The automated EBE method proposed in [25] sequentially generates a number of subsets by randomly selecting pixels from the observations, extracts endmembers from each subset, then integrates all of the extracted endmembers as the final endmember bundles. The above methods can extract endmember bundles with high efficiency. However, they do not consider spatial information, and they cannot guarantee that endmembers appear in each subset, which may result in the presence of mixed pixels in the extracted endmembers. To enhance the ability of EBE, Xu *et al.* [26] proposed an image-based EBE method using both spatial and spectral information (SSEBE). SSEBE uses PPI to select candidate endmembers. Since it takes all pixels that have a positive PPI index as candidate endmembers, there is a high probability that the candidate set contains mixed pixels. To solve this problem, SSEBE uses a homogeneity index (HI) to retain the candidate endmembers that are spectrally similar to their spatially adjacent pixels as final endmember bundles. Another work of Xu *et al.* [27] also utilizes PPI to select candidate endmembers, removing the mixed and redundant endmembers by analyzing the reconstruction error between the chosen endmembers and the remaining candidate endmembers. The effectiveness of these two methods largely depends on the quality of the candidate endmember set. However, the geometric structure of a real HSI in the feature space is not a simple simplex and endmembers may locate within the boundary of the simplex; PPI may fail to extract those endmembers, resulting in an incomplete candidate endmember set.

The convex geometry-based methods proposed in [28] and [29] have the same difficulty of extracting endmembers present within the boundary of the data simplex. The spectral curve-based endmember extraction (SCEE) method [30] obtains spectral curves by processing the original observed data with wavelet transform with different scale factors, and chooses a user-defined number of pixels with maximal or minimal values in each dimension of the curves as candidate endmembers. SCEE uses connected-component labeling to remove mixed pixels from candidate endmembers: an endmember region with an area of more than eight pixels is retained and candidate endmembers that locate outside of the region are removed. SCEE can extract complete candidate endmember sets when the user-defined number of pixels is large enough, which may lead to high redundancy. Furthermore, rare pure pixels may be removed in the mixed pixel removal step.

In recent years, intelligent optimization has been successfully applied in EE. These methods consider EE to be a combinatorial optimization problem and use different strategies to optimize the designed objective functions [31]–[36]. The first work applying intelligent optimization in EE was proposed by Zhang *et al.* [31], who took the minimization of root-mean-square error (RMSE) between the original image and the reconstructed image as the objective function and used discrete particle swarm optimization to search the optimal endmember combination. Du *et al.* [37] systematically constructed a quantum behavior-driven particle swarm optimization algorithm to effectively extract endmembers from HSIs. Other strategies, such as ant colony optimization and genetic optimization, have also been employed to minimize the RMSE [33], [36]. It has been proven that intelligent optimization-based methods can obtain results with smaller RMSE than traditional EE methods. Another objective function used in the intelligent optimization-based methods is the maximization of the volume of the simplex constructed by the chosen endmembers. It has been shown that the EE results obtained by these two objective functions are different [38]. In order to get robust results for different real images, multiobjective optimization is used to simultaneously optimize the two objective functions [39], [40]. Although the existing optimization-based EE methods have achieved better results than the traditional EE methods, they do not consider the endmember variability problem, which cannot best fit the situation of real HSIs.

This article proposes a new method to enhance the performance of EBE by leveraging the outstanding optimization ability of intelligent optimization. The proposed method is called multiobjective endmember bundle extraction (MOEBE). For the real HSI, the observed data in the feature space is usually not a simple simplex. It is easy to lose some of the endmembers if the EE is operated in a single dataspace. Considering that different materials have different characteristics among different wavelength ranges, we divide the original data equally into three subsets along its spectral dimension. The feature spaces of these three subsets are different, which means that the distribution of endmembers may differ in the three dataspaces. Even so, the pixels that locate on the vertices of the data simplex for all three subsets are endmembers. The idea of the proposed work is to simultaneously operate EE on the three constructed spaces to obtain multiple endmembers with variability. The simplex volume is used to measure the positions of the endmembers, and the objective function is used to simultaneously maximize the volume of the simplex constructed by endmembers from each subset. A set of Pareto solutions will be obtained by a modified multiobjective particle swarm optimization method [41], and the Pareto solutions can be integrated to produce candidate endmembers. To remove the possible mixed pixels and redundant endmembers from the candidate set, a post-processing step inspired by the technique used in SSEBE [26] as well as the sequential forward floating selection (SFFS) method [42] are utilized to reach the final result. The main contributions of this work can be summarized as follows:

1) Unlike existing EBE methods that only operate EE in a single feature space, the proposed method jointly operates in multiple feature spaces to obtain multiple endmembers. In multiple feature spaces, more endmembers will be located in the vertices of the data simplex, which

will benefit the completeness of the extracted multiple endmembers.

2) The multiobjective particle swarm optimization method is modified to better fit the problem. Specifically, the coding of the particles and searching strategy of the population are designed based on the characteristics of the HSI, which helps to find the optimal solution and accelerate the optimization process.
3) Both the endmembers located in the vertices of the data simplex and those located within the boundary of the data simplex can be extracted by taking advantage of the Pareto solutions. As long as the endmember combination is not dominated by other combinations, it is a Pareto solution and they will be taken as candidate endmembers. In fact, this kind of endmember combination can also contain endmembers located within the boundary of the simplex. Therefore, the endmembers located within the boundary of the simplex can be extracted by the proposed method.

This article is structured as follows. Section II briefly introduces the linear mixture model (LMM) and multiobjective optimization. Section III gives a detailed description of the proposed method. Section IV describes the comparison experiments between MOEBE and several representative EBE algorithms, with both synthetic HSIs and real data sets. The conclusion is given in Section V.

II. Related Works

A. Linear Mixture Model

The LMM [43] is widely used in HU. The majority of existing EE methods are based on the LMM. In the LMM, a mixed pixel is assumed to be the linear combination of all its constituent materials and the corresponding abundance coefficients. Suppose that the image contains N pixels with L spectral bands, and let $\mathbf{y} = (y_1, y_2, \ldots, y_L)^{\mathrm{T}}$ be one of the N pixel vectors. Without considering endmember variability, the spectral signature $\mathbf{y}$ can be represented by the LMM as follows:

$$\mathbf{y} = \sum_{i=1}^{P} s_i \mathbf{a}_i + \mathbf{e} = \mathbf{A}\mathbf{s} + \mathbf{e} \tag{1}$$

where $\mathbf{A} = [\mathbf{a}_1, \mathbf{a}_2, \ldots, \mathbf{a}_P]$ denotes the $L \times P$ endmember matrix, with $\mathbf{a}_i = (a_1, a_2, \ldots, a_L)^{\mathrm{T}}$ being the ith endmember signature, and P is the number of endmembers. The expression $\mathbf{s} = (s_1, s_2, \ldots, s_P)^{\mathrm{T}}$ is a P-dimensional vector associated with $\mathbf{y}$, and s_i denotes the abundance fraction of the ith endmember present in the pixel $\mathbf{y}$. The term $\mathbf{e}$ represents the $L \times 1$ additive observation noise and error vector. The LMM for all the observed pixels can be expressed by the matrix notation as

$$\mathbf{Y} = \mathbf{A}\mathbf{S} + \mathbf{E} \tag{2}$$

where $\mathbf{Y} = [\mathbf{y}_1, \mathbf{y}_2, \ldots, \mathbf{y}_N]$, $\mathbf{S} = [\mathbf{s}_1, \mathbf{s}_2, \ldots, \mathbf{s}_N]$, and $\mathbf{E} = [\mathbf{e}_1, \mathbf{e}_2, \ldots, \mathbf{e}_N]$. The abundance is subject to two constraints with the physical meaning: the abundance nonnegative constraint (ANC) and the abundance sum-to-one constraint (ASC), which can be given by $s_i \geq 0, i = 1, 2, \ldots, P$ and $\mathbf{1}^{\mathrm{T}}\mathbf{s} = 1$, respectively.

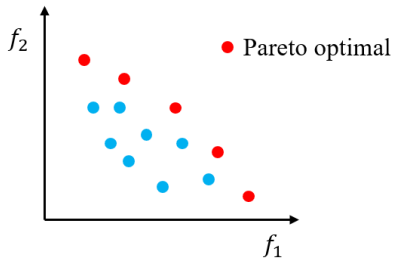

Fig. 1. Example of the Pareto optimal for the maximization optimization.

If the endmember variability problem is considered, we can use endmember bundles that contain multiple endmember spectra with variability within each endmember class to substitute the corresponding endmember spectra in (1). The endmember bundle matrix is denoted by $\mathbf{B}$ in this article.

B. Multiobjective Optimization

Considering the maximization optimization problem, a multiobjective optimization problem can be expressed as

$$\max\ f(\mathbf{z}) = [f_1(\mathbf{z}), f_2(\mathbf{z}), \ldots, f_m(\mathbf{z})] \tag{3}$$

where the decision vector $\mathbf{z}$ belongs to the feasible solution space and $m(\geq 2)$ conflicting objective functions are to be maximized simultaneously. A decision vector $\mathbf{z}_2$ is said to be dominated by $\mathbf{z}_1$ if

$$\forall i \in [1, 2, \ldots, m], \quad f_i(\mathbf{z}_1) \geq f_i(\mathbf{z}_2),\ \exists f_i(\mathbf{z}_1) \neq f_i(\mathbf{z}_2). \tag{4}$$

A vector $\mathbf{z}_1$ is called Pareto optimal if it is not dominated by any other vectors. Fig. 1 shows the Pareto optimal solutions in the objective space when $m = 2$. It is obvious that Pareto optimal solutions are nondominated solutions. There is no single optimal solution for multiobjective optimization problems. The results of the multiobjective optimization are a set of Pareto optimal solutions. The corresponding objective vector set of all Pareto optimal solutions is called the Pareto front, and the task of multiobjective optimization is to achieve the Pareto optimal solutions.

C. Evolutionary Algorithm

In the past decades, evolutionary algorithms have attracted increasing interest for the solution of multiobjective optimization problems and a large number of multiobjective evolutionary algorithms (MOEAs) have been developed, including genetic algorithm [44]–[46], differential evolution [47], [48], particle swarm optimization [41], [49], [50], and memetic algorithm [51]–[53]. The goal of MOEA is to reach a good distribution of Pareto solutions with good convergence and diversity. An MOEA usually maintains a population consisting of a set of individuals, where an individual represents a solution to the problem. The individuals are generated by operators and the population is updated in each generation of the evolution to approach the optimal result. Most of

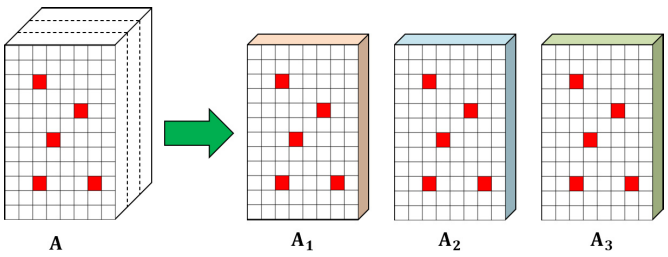

Fig. 2. Division of the image cube and the endmembers of each subset. The red squares denote endmembers.

the MOEAs mainly focus on three categories. One category contains the decomposition-based algorithms such as those proposed in [54]–[56]. The second category is the indicator-based approach such as [57]–[59]. The Pareto domination approaches [60], [61] belong to the third category.

The competition mechanism-based multiobjective particle swarm optimization (CMOPSO) algorithm [41], which belongs to the Pareto domination approach, is adopted as the basic optimization model for the multiobjective EBE problem due to the high convergence speed and simple implementation. In particle swarm optimization, a particle searches in the feasible solution space by moving along a trajectory depicted by its position and velocity until reaching the optimal. In CMOPSO, a competition mechanism-based learning strategy is used for the updating of particles. In this strategy, particles are pairwise randomly selected from the current swarm for competition. The loser in the competition is updated by learning from the winner, whereas the winner is directly passed to the swarm of next generation. The elite particles, which are used to provide candidate particles to be used in the pairwise competitions to guide the search of the swarm, are selected by the nondominated sorting and crowding distance-based ranking as adopted in nondominated sorting genetic algorithm (NSGA)-II [62].

III. EBE Based on Multiobjective Particle Swarm Optimizer

The proposed MOEBE method implements the task of EBE through a modified multiobjective particle swarm optimizer and seeks to find the Pareto optimal solutions of multiple objective functions in order to obtain candidate endmembers with variability. The final results are obtained after removing the mixed pixels and redundant endmembers. In the following, we will introduce the method in detail.

A. Objective Functions

In the convex geometry-based EE methods, volume maximization is quite often utilized to extract endmembers. It assumes that the vertices of the simplex with the largest volume are endmembers. In MOEBE, the original image cube is divided into three subsets along the spectral dimension, as shown in Fig. 2. The volume maximization objective function is applied for each subset as follows:

$$\max\ f_i = \text{volume}(\mathbf{A}_i) = \frac{\left|\det\begin{bmatrix}\mathbf{1}^{\mathrm{T}}\\ \widetilde{\mathbf{A}}_i\end{bmatrix}\right|}{(P-1)!},\quad i=1,2,3 \tag{5}$$

where $\mathbf{A}_i (i = 1, 2, 3)$ are endmember matrices of each subset. In order to calculate the volume, the dimensionality of endmember matrices $\mathbf{A}_i (i = 1, 2, 3)$ is reduced to $P - 1$ by minimum noise fraction (MNF) [63]; $\widetilde{\mathbf{A}}_i (i = 1, 2, 3)$ are the dimensionality reduced matrices.

The motivation of dividing the image cube into subsets is that the observed data in the feature space is no longer a simple simplex if there exists endmember variability. In this situation, endmembers may locate within the boundary of the data simplex, which makes the extraction of these endmembers difficult. The division into subsets enables us to operate in multiple spaces, making it possible to solve the variability problem. A set of synthetic pixels is generated to show the mechanism of MOEBE. The endmembers are chosen from the United States Geological Survey (USGS) spectral library, which are montmorillonite, calcite, and topaz, as shown in Fig. 3. Abundance fractions are generated according to the Dirichlet distribution. To display the pixels in feature spaces, dimensionality reduction is implemented on all the pixels by MNF. The structures of both the original data and the three subsets are shown in Fig. 4. It is clear that both the structure of the data and the locations of endmembers are different, which indicates that operating EE in multiple spaces would be useful.

B. MOEBE Procedure

A modified multiobjective particle swarm optimization algorithm based on CMOPSO is employed to optimize the designed objective functions. For the EE problem, the feasible solution space is discrete, accordingly the particle's position must be discrete. Spatial locations of endmembers are used to code the position of particles. The position of a particle can be written as

$$X = (X_{r1}, X_{r2}, \ldots, X_{rP}, X_{c1}, X_{c2}, \ldots, X_{cP}) \tag{6}$$

where X_{ri} $(i = 1, 2, \ldots, P)$ is the row number of the ith endmember, and X_{ci} $(i = 1, 2, \ldots, P)$ is the column number of the ith endmember. With the row and column numbers, we can accordingly build a combination of endmembers, which is a feasible solution to the EE problem. The velocity of a particle can be written as

$$V = (V_{r1}, V_{r2}, \ldots, V_{rP}, V_{c1}, V_{c2}, \ldots, V_{cP}). \tag{7}$$

The competition mechanism used in CMOPSO is not adopted by the proposed method. In MOEBE, we have designed two kinds of particles, one that performs experienced searching and another that performs local searching. The number of particles for the two kinds is the same, and the total number of particles is denoted by M. Assuming the velocity and position of a particle at the current time are V_{old} and X_{old}, and the velocity and position of a particle at the next time are V_{new} and X_{new}. The update of velocity based on the experienced searching is

$$V_{\text{new}} = \text{round}(r_1 V_{\text{old}} + r_2(X_b - X_{\text{old}})) \tag{8}$$

where r_1 and r_2 are random numbers in the interval $(0, 1)$. The term X_b is the historical best solution of the particle.

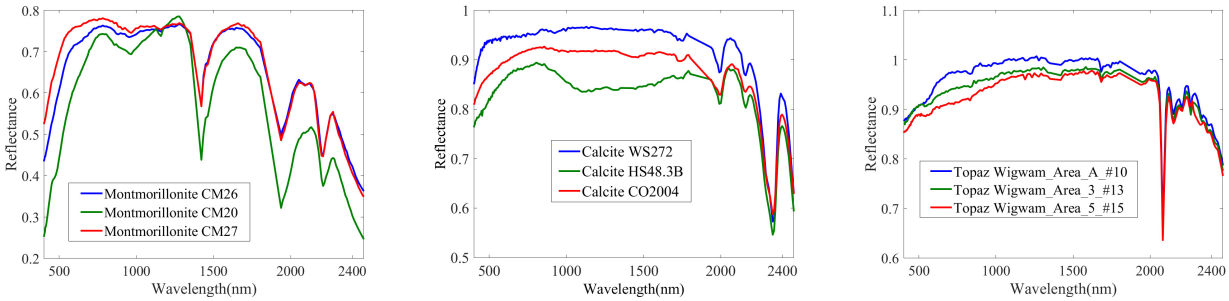

Fig. 3. Endmembers used to generate synthetic pixels.

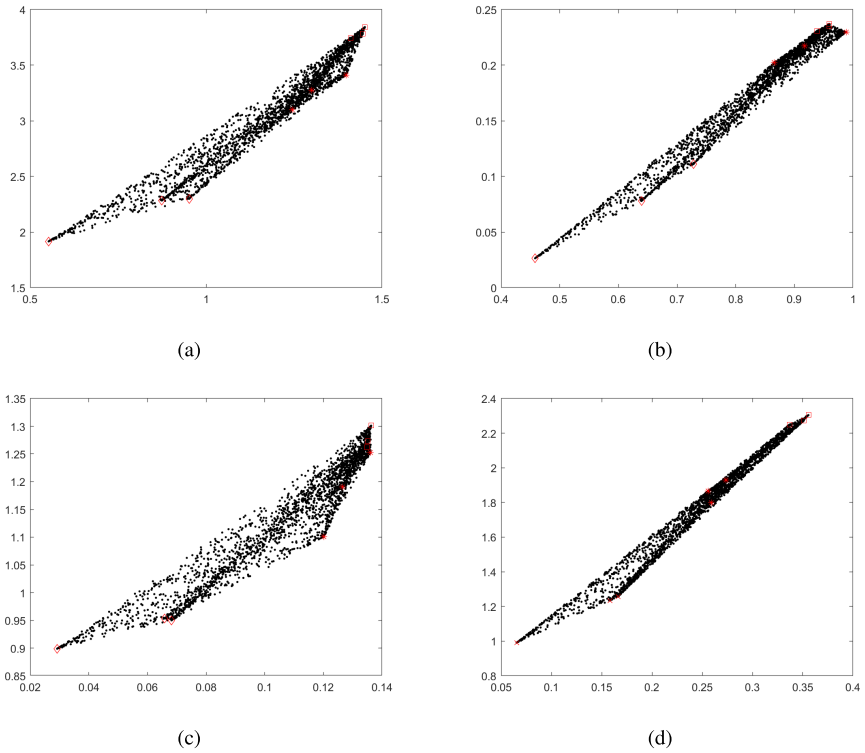

Fig. 4. Distribution of pixels in feature spaces. The red marks of diamond, asterisk, and square represent endmembers of montmorillonite, calcite and topaz, respectively. (a) Data distribution of the original image. (b) Data distribution of the first subset. (c) Data distribution of the second subset. (d) Data distribution of the third subset.

The round() operation rounds each element to the nearest integer. The update of velocity based on the local searching is

$$V_{\text{new}} = R([-5, 5]) \tag{9}$$

where the operation of R is to randomly choose values from the integers in the interval $[-5, 5]$. This operation makes the particle search in a local window with the size 5×5. The position of the particle is updated by

$$X_{\text{new}} = X_{\text{old}} + V_{\text{new}}. \tag{10}$$

According to the definition of the particle's position, there should be a lower bound and an upper bound for each element of the position. If the spatial size of the image is $r \times c$, then the lower band is 1 and the upper bound is r for the first P elements, and the lower band is 1 and the upper bound is c for the last P elements. To accelerate the optimization process, the endmembers extracted by VCA are used to initialize a part of the endmembers as [37] did. In order to increase the diversity of the population, the polynomial mutation operator in [64] is used after the update of particles. Nondominated sorting [60] is utilized to choose the optimal solutions. The nondominated solutions are saved in the archive $gbest$. When the number of solutions in the archive is greater than M, we calculate the product of three objective function values for each solution and only keep the first M solutions with larger values to avoid explosion. Multiobjective particle swarm optimization is an iterative process. The maximum number of iterations max_iter is used as the stopping condition for the optimization process. All the solutions in the final archive constitute the candidate endmember set. The optimization results of independent runs of the multiobjective particle swarm optimization method are different due to the

Algorithm 1 Multiobjective Particle Swarm Optimization

1: Set the lower bound and the upper bound of the position of the particles: $X_l = \text{ones}(1, D)$, where $D = 2 \times P$, $X_u = [r \times \text{ones}(1, P), c \times \text{ones}(1, P)]$. Set $t = 0$ and $gbest = \emptyset$.
2: Randomly initialize the position of each particle with values being within the lower bound and the upper bound; initialize the velocity of each particle with all zero elements. Perform VCA to each subset $\mathbf{Y}_i, i = 1, 2, 3$, and substitute the positions of the first three particles with those extracted by VCA. Calculate the three objective function values for all particles. Initialize the best position of each particle X_b.
3: For each particle with experienced searching, update the velocity by (8); for each particle with local searching, update the velocity by (9).
4: Update the position of each particle by (10), and set the elements to valid range by $X_{new} = min(max(X_{new}, X_l), X_u)$.
5: Perform the polynomial mutation.
6: Calculate the three objective function values for each particle.
7: Do nondominated sorting on the objective function values. If X_{new} is not dominated by X_{old}, then $gbest = gbest \cup X_{new}$. Update X_b.
8: If the size of $gbest$ is larger than M, then only keep the first M solutions with larger prod$(f_i(gbest), i = 1, 2, 3)$.
9: $t = t + 1$.
10: If $t \leq max\_iter$, go to step 3, otherwise output $gbest$.
11: Find the corresponding endmembers from $\mathbf{Y}$ according to $gbest$, and obtain the endmember candidates $\mathbf{B}$.

intrinsic mechanism of the method. To ensure the stability of the results, ten independent runs are implemented and the candidate endmember set comes from the integration of the results. The procedure of the multiobjective particle swarm optimization method is shown in **Algorithm 1**.

To show that nondominated solutions can help to extract endmembers with variability, we calculated the objective function values of all the endmember combinations among different endmember classes from Fig. 3; the results are displayed in Table I. The endmembers of montmorillonite, calcite, and topaz are denoted by m, c, and t, respectively, and index values $1, 2, 3$ are used to distinguish different endmembers within an endmember class. All the nondominated combinations are displayed in bold. It can be seen that the union set of all nondominated solutions contains all of the nine endmembers, which means that we can successfully achieve the endmember candidate set containing all the endmembers if the nondominated solutions are obtained by multiobjective optimization.

TABLE I
OBJECTIVE FUNCTION VALUES OF COMBINATIONS AMONG ENDMEMBER CLASSES MONTMORILLONITE, CALCITE, AND TOPAZ, NONDOMINATED SOLUTIONS ARE SHOWN IN BOLD

Endmember combinations	f_1	f_2	f_3
(m_1, c_1, t_1)	1.16E-03	5.42E-04	2.49E-03
(m_1, c_1, t_2)	1.04E-03	2.85E-04	2.54E-03
$\mathbf{(m_1, c_1, t_3)}$	**1.32E-03**	**1.73E-04**	**1.36E-03**
(m_1, c_2, t_1)	6.35E-04	1.33E-03	9.11E-04
(m_1, c_2, t_2)	7.14E-04	1.12E-03	9.87E-04
$\mathbf{(m_1, c_2, t_3)}$	**4.44E-04**	**1.03E-03**	**5.71E-05**
(m_1, c_3, t_1)	5.88E-05	6.83E-04	3.62E-03
(m_1, c_3, t_2)	1.56E-04	4.59E-04	3.62E-03
$\mathbf{(m_1, c_3, t_3)}$	**1.30E-04**	**3.61E-04**	**2.52E-03**
(m_2, c_1, t_1)	1.63E-03	8.58E-04	2.02E-04
$\mathbf{(m_2, c_1, t_2)}$	**1.45E-03**	**4.29E-04**	**1.78E-04**
(m_2, c_1, t_3)	1.78E-03	2.46E-04	1.25E-03
(m_2, c_2, t_1)	3.90E-04	2.50E-03	3.32E-03
(m_2, c_2, t_2)	5.32E-04	2.12E-03	2.92E-03
(m_2, c_2, t_3)	2.10E-04	1.96E-03	4.10E-03
$\mathbf{(m_2, c_3, t_1)}$	**1.78E-04**	**1.32E-03**	**6.65E-04**
$\mathbf{(m_2, c_3, t_2)}$	**1.70E-05**	**9.22E-04**	**9.99E-04**
$\mathbf{(m_2, c_3, t_3)}$	**3.55E-04**	**7.54E-04**	**3.50E-04**
$\mathbf{(m_3, c_1, t_1)}$	**8.94E-04**	**5.61E-04**	**2.29E-03**
$\mathbf{(m_3, c_1, t_2)}$	**8.03E-04**	**2.93E-04**	**2.37E-03**
$\mathbf{(m_3, c_1, t_3)}$	**1.03E-03**	**1.76E-04**	**1.16E-03**
(m_3, c_2, t_1)	6.30E-04	1.42E-03	5.92E-04
(m_3, c_2, t_2)	6.78E-04	1.20E-03	6.93E-04
(m_3, c_2, t_3)	4.61E-04	1.10E-03	2.59E-04
(m_3, c_3, t_1)	1.19E-04	7.32E-04	3.40E-03
(m_3, c_3, t_2)	1.85E-04	4.96E-04	3.43E-03
$\mathbf{(m_3, c_3, t_3)}$	**4.81E-05**	**3.94E-04**	**2.31E-03**

C. Removal of Mixed Pixels and Redundant Endmembers

Spatial post-processing is utilized to remove mixed pixels from the candidate endmembers. MOEBE adopts the post-processing method used in [26] but uses a slightly different approach. Its steps are: 1) calculate the spectral angle distance (SAD) between each candidate endmember and its spatially neighboring pixels within a 5×5 window and keep the maximum SAD for each candidate endmember and 2) show the histogram of the SAD for all candidate endmembers and determine a threshold value τ according to the histogram. The candidate endmembers with maximum SAD larger than the threshold are then removed. After the spatial post-processing, the candidate endmember set is updated to $\mathbf{B}_1$.

The post-processing is a rough screening and can only remove some mixed pixels. In addition to the spatial post-processing, the SFFS method is utilized to further remove mixed pixels and redundant endmembers. Spatial post-processing is applied before SFFS because SFFS is time consuming: it saves time if the size of candidate endmember set is reduced in advance.

The aim of the SFFS-based method is to select a subset from the endmember candidate set. Two criterion functions are required to search the optimal subset. One examines the significance of a new endmember, while the other tests if the newly selected endmember can replace some of existing endmembers and form a downsized subset with a higher performance score than that for the same size subset. The criterion function for identifying a new endmember is expressed as

$$J_1(\overline{B}_k) = \text{error1}(\overline{B}_k, B_k) = [e_1, \ldots, e_i, \ldots, e_{(K_1-k)}]$$
$$e_i = \sqrt{\frac{1}{L}\|\mathbf{b}_i - \hat{\mathbf{b}}_i\|_2^2} \tag{11}$$

where B_k is the set of k selected endmembers, $\overline{B}_k$ is the remaining set of endmembers after removing k endmembers

Algorithm 2 SFFS-Based Endmember Selection

1: Identify two initial endmembers. The first endmember $\mathbf{b}_1$ is selected as the one in $\mathbf{B}_1 \in R^{L\times K_1}$ that yields the maximum norm: $\mathbf{b}_1 = \arg\{\max[\|\mathbf{b}\|_2^2]\}$. The second endmember $\mathbf{b}_2$ is the one in $\overline{B}_k$ that has the biggest distance with $\mathbf{b}_1$: $\mathbf{b}_2 = \arg\{\max[\|\mathbf{b}-\mathbf{b}_1\|_2^2]\}$. Update B_k and $\overline{B}_k$.
2: Select the endmember corresponding to the largest $J_1(\overline{B}_k)$ value as the candidate of *(k+1)*th endmember $\mathbf{b}_{new}$ and set $B_{k+1} = B_k + \mathbf{b}_{new}$.
3: If $J_2(B_{k+1}-\mathbf{b}_{new}) \le \min_{1<j<k} J_2(B_{k+1}-\mathbf{b}_j)$, then set $k = k+1$ and return to step 2, else exclude $\mathbf{b}_j, 1 < j < k$ from B_{k+1} to form a new endmember set $B'_k = B_{k+1} - \mathbf{b}_j$. If $k = 2$, then set $B_k = B'_k$ and return to step 2, else go to step 4.
4: If $J_2(B'_k-\mathbf{b}_{new}) \le \min_{1<j<k-1} J_2(B'_k-\mathbf{b}_j)$, then set $B_k = B'_k$ and return to step 2, else exclude $\mathbf{b}_j, 1 < j < k-1$ from B'_k to form a newly reduced set $B'_{k-1} = B'_k - \mathbf{b}_j$, set $k = k-1$. Now $B_k = B'_k$. Return to step 2.
5: The termination condition for step 2 $\sim$ 4 is: $k \ge 3$ and $abs((J_2(B_{k-2})-J_2(B_{k-1}))-(J_2(B_{k-1})-J_2(B_k))) < \omega$.
6: Output the selected endmembers $\mathbf{B}_2$ that contains in the set B_k.

from $\mathbf{B}_1$. The term K_1 is the number of candidate endmembers in $\mathbf{B}_1$, $\mathbf{b}_i$ is the ith endmember in $\overline{B}_k$, and $\hat{\mathbf{b}}_i$ is the reconstructed spectrum of $\mathbf{b}_i$ by using the endmembers in B_k and the nonnegative constrained least square (NCLS) method [65]. The reconstruction error for the ith endmembers in $\overline{B}_k$ is denoted by e_i.

The criterion function for testing the newly selected endmembers is expressed as

$$J_2(B_k) = \text{error2}(\mathbf{B}_1, B_k) = \frac{1}{K_1}\sum_{i=1}^{K_1}\sqrt{\frac{1}{L}\|\mathbf{b}_i - \hat{\mathbf{b}}_i\|_2^2} \quad (12)$$

where $\hat{\mathbf{b}}_i$ is the reconstructed spectrum of $\mathbf{b}_i$ by using the endmembers in B_k and the NCLS method. The term $\mathbf{b}_i$ is the ith endmember in $\mathbf{B}_1$. The procedure of the SFFS-based endmember selection method is described in **Algorithm 2**.

D. Overall Workflow of MOEBE

The overall workflow of the proposed MOEBE method is shown in **Algorithm 3**.

Algorithm 3 MOEBE

Input: Hyperspectral imagery $\mathbf{Y} \in R^{r\times c\times L}$. The number of particles M, where half of the particles do experienced searching, and half do local searching. The number of endmembers P. The maximum number of evaluations max_iter. The threshold ω for removing redundant endmembers.

Output: Multiple endmembers with variability.

Step 1: Division of the input hyperspectral imagery along the spectral dimension

The observed data $\mathbf{Y} \in R^{r\times c\times L}$ is divided into three subsets: $\mathbf{Y}_i \in R^{r\times c\times L_i}, i = 1,2,3, \sum_{i=1}^{3} L_i = L$, where the number of bands for each subset is the same if L is divisible by 3, otherwise the remainder are added to the third subset.

Step 2: Dimensionality reduction of the subsets

Apply the MNF transformation to the input hyperspectral data $\mathbf{Y}$ to obtain the transformation matrix.

Use the corresponding parts of the transformation matrix to perform dimensionality reduction for $\mathbf{Y}_i, i = 1,2,3$, generating the data $\widetilde{\mathbf{Y}}'_i \in R^{r\times c\times P-1}, i = 1,2,3$.

A row with all elements equal to 1 is added to $\widetilde{\mathbf{Y}}'_i, i = 1,2,3$, constructing data $\widetilde{\mathbf{Y}}_i \in R^{r\times c\times P}, i = 1,2,3$ that is used to calculate the volume.

Step 3: Selection of endmembers by MOEBE

Perform MOEBE in **Algorithm 1** to get the candidate endmembers $\mathbf{B} \in R^{L\times K}$.

Step 4: Removal of mixed pixels and redundant spectra from candidate endmembers

Perform spatial post-processing to get a downsized endmember candidate set $\mathbf{B}_1 \in R^{L\times K_1}$.

Perform SFFS in **Algorithm 2** to get the final result $\mathbf{B}_2 \in R^{L\times K_2}$.

IV. Experiments and Analysis

A. Data for Experiments

Four data sets were used to validate the proposed method. One of them was simulated by library endmembers and synthetic abundance fractions. The other three were real images: the Samson data set, the Jasper Ridge data set, and the Urban data set.

A synthetic data set was used for experiments because it enabled methods to be precisely validated using known endmembers and abundances. The endmembers used to generate the synthetic data were chosen from the USGS spectral library, including 12 endmember classes as shown in Fig. 5. The abundances with size 200 × 200 were generated by the "synthesis tools" package, which is a MATLAB toolbox available online.[1] The abundance maps for the 12 endmember classes are displayed in Fig. 6. To generate synthetic pixels, a single spectrum was randomly selected from multiple endmember spectra for each endmember class, and these selected endmembers were linear combined weighted by the corresponding abundance fractions to produce the synthetic spectral mixture. White Gaussian noise with SNR of 50 dB was added to the synthetic data.

Samson is a simple data set. A region of 95 × 95 pixels was used for this experiment, as shown in Fig. 7(a). Each pixel is recorded with 156 spectral bands covering the wavelengths from 401 to 889 nm. There are three main endmember classes in this image, i.e., soil, tree, and water.

The Jasper Ridge data set used for this experiment contains 100 × 100 pixels, as shown in Fig. 7(b). The wavelength ranges from 380 to 2500 nm. After removing the water absorption and noisy bands (1–3, 108–112, 154–166, and 220–224)

[1] [Online]. Available: http://www.ehu.es/ccwintco/index.php/Hyperspectral_Imagery_Synthesis_tools_for_MATLAB

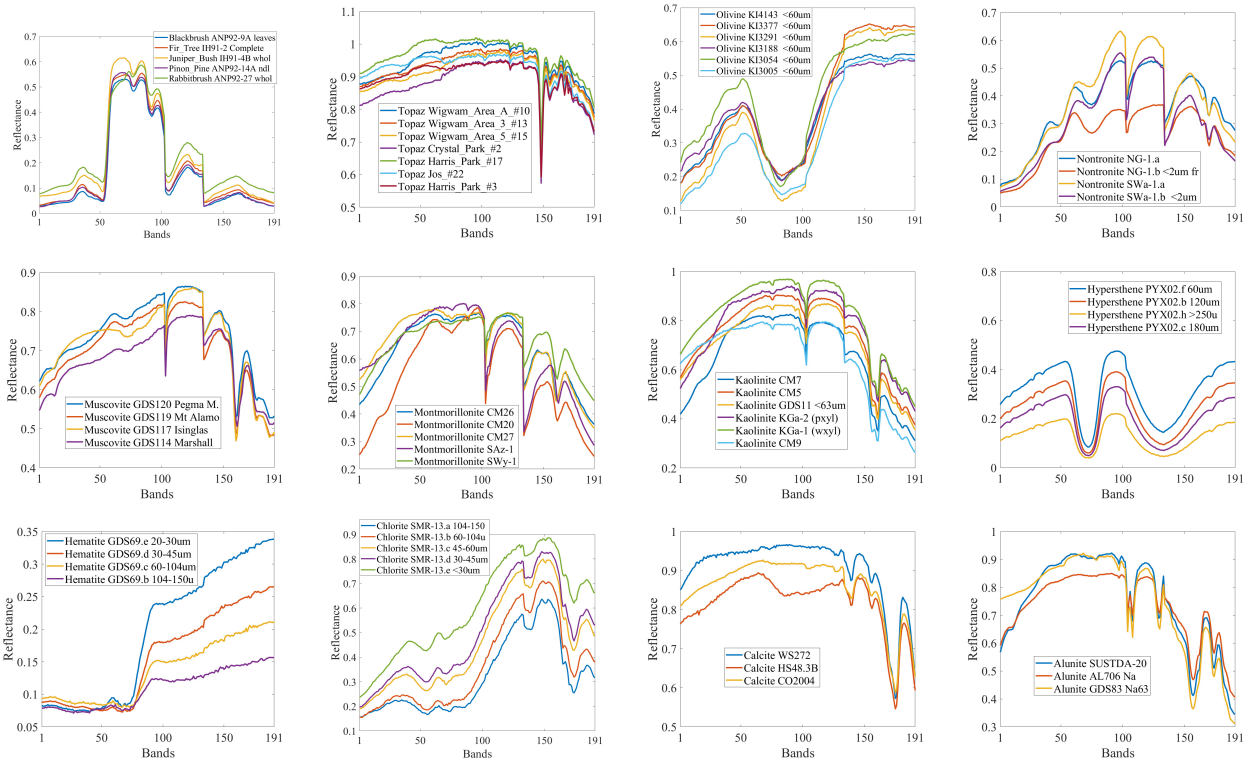

Fig. 5. Synthetic multiple endmember spectra of each endmember class.

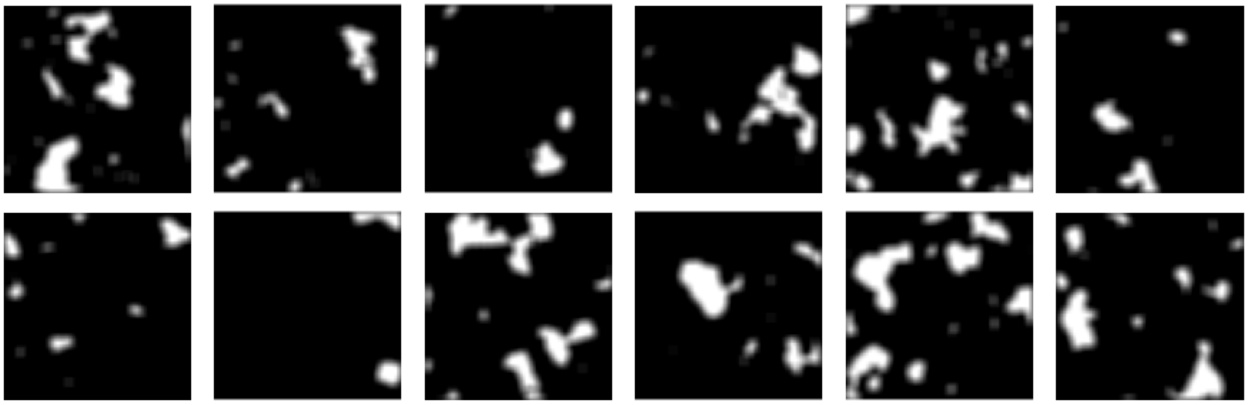

Fig. 6. Synthetic abundance maps of each endmember class.

from the original 224 bands, the remaining 198 bands were used for the experiment. There are four main endmember classes in this data: road, soil, water, and tree.

Urban is one of the most widely used hyperspectral data used in the HU study and is shown in Fig. 7(c). There are 307×307 pixels. The wavelength ranges from 400 to 2500 nm. After removing the water absorption and noisy bands (1–4, 76, 87, 101–111, 136–153, and 198–210) from the original 210 bands, the remaining 162 bands were used for the experiment. The number of endmember classes was set to 6 for this experiment: asphalt road, grass, tree, roof#1, roof#2, and soil.

B. Performance Metrics

Four metrics, SAD, RMSE, average deviation of the mean (ADM), and average deviation of the standard deviations (ADS), were used for quantitative validation [30]. SAD measures the SAD between each extracted endmember and the reference endmember. RMSE is the root-mean-square error between estimated abundances and true abundances. ADM is the average deviation between the mean of the reference endmembers for each endmember class and the mean of the extracted endmembers for each endmember class. ADS is the average deviation between the standard deviations of the reference endmembers for each endmember class and the standard deviations of the extracted endmembers for each endmember class. Smaller values of the four metrics indicate better results. The true endmembers and abundances of the synthetic data were known. The reference endmembers and abundances of the three real images were provided by Zhu *et al.* [66]–[68], and are available online.[2] Abundances were estimated by sparse unmixing via the variable splitting and

[2][Online]. Available: https://sites.google.com/site/feiyunzhuhomepage/data sets-ground-truths

(a) (b) (c)

Fig. 7. Three real HSIs. (a) Samson. (b) Jasper Ridge. (c) Urban.

augmented Lagrangian (SUnSAL) method [69] for all the experiments. The extracted multiple endmembers were not clustered into bundles by any clustering algorithm. Instead, they were compared with the reference endmembers by calculating the SAD between the extracted endmember and each reference endmember; the extracted endmember was then assigned to the endmember class with the smallest SAD. The abundance map for one endmember class was the sum of the abundances of all the endmembers within the endmember class.

All four of the metrics were used to evaluate performance for the synthetic experiments, whereas only SAD and RMSE were used for the real image experiments. This was because references of the synthetic data are endmember classes with variability, whereas there is only one reference spectrum for one class for the real data sets.

C. Methods Used for Comparison With MOEBE and Parameter Settings

The EBE [25], SSEBE [26], and SCEE [30] methods were used for comparison with MOEBE. All four methods required parameters. For EBE, the number of subsets and the percentage of the pixel number of subsets against the pixel number of the original image are required parameters. For SSEBE, the block size and the percentage of endmembers in each block are required parameters. For SCEE, the user-defined number of endmember candidates is the required parameter. For MOEBE, the number of particles, the maximum number of iterations, and the threshold for the SFFS method are required parameters. The number of particles and the maximum number of iterations were empirically set to 40 and 2000, respectively, for all the experiments, and only the threshold for the SFFS method was tested and specially determined for each experimental data set. All parameters were determined for each data set by choosing parameters that generated the best result in terms of SAD and ADS for the synthetic data set, and in terms of SAD and RMSE for the three real data sets.

For EBE, parameter combinations of the number of subsets (30, 50, 70, 90, 110) and the percentage of subsets (0.05, 0.1, 0.15, 0.2, 0.3, 0.4, 0.5) were tested. Optimal parameter combinations were 30 and 0.2 for the synthetic data set, 90 and 0.05 for the Samson data set, 110 and 0.05 for the Jasper Ridge data set, and 110 and 0.05 for the Urban data set. For SSEBE, parameter combinations of the block size (15, 25, 35, 45, 55) and the percentage of endmembers in each block (0.01, 0.02, 0.03, 0.04, 0.05, 0.1, 0.2, 0.3) were tested. Optimal parameter combinations were 35 and 0.05 for the synthetic data set, 35 and 0.3 for the Samson data set, 15 and 0.05 for the Jasper Ridge data set, and 15 and 0.05 for the Urban data set. For SCEE, parameters of user-defined number of endmember candidates (30, 50, 70, 90, 110, 130, 150) were tested. Optimal parameters were 150 for the synthetic data set, 50 for the Samson data set, 50 for the Jasper Ridge data set, and 90 for the Urban data set. For MOEBE, parameters of the threshold for SFFS (10^{-6}, 10^{-7}, 10^{-8}, 10^{-9}, and 10^{-10}) were tested. Optimal parameters were 10^{-7} for the synthetic data set, and 10^{-8} for the three real data sets.

D. Results

1) Results of Experiment 1 (Using the Synthetic Data Set): To validate the effectiveness of the velocity and position updating strategies used in MOEBE, the velocity and position updating strategies of the proposed method are replaced with the original ones in CMOPSO (named as MOEBE_CM), and the method has been tested on the synthetic image. The comparison results of SAD, RMSE, ADS, and ADM from MOEBE and MOEBE_CM are shown in Fig. 8. The proposed velocity and position updating strategies produced better results than that of CMOPSO, which demonstrated the effectiveness of the proposed method.

In experiment 1, the endmembers extracted by EBE, SSEBE, SCEE, and MOEBE were evaluated quantitatively with SAD, RMSE, ADS, and ADM under the condition that the true endmembers with variability and abundances were known. Ten independent runs were implemented for each method in order to test the stability of each method. The mean and standard deviations of SAD, RMSE, ADS, and ADM of the ten runs are recorded in Table II, and are also shown in the form of a bar graph in Fig. 9. Positive feedback for the stability of each method was received from the small standard

TABLE II
QUANTITATIVE EVALUATION RESULTS OF SYNTHETIC DATA SET

Method	SAD	RMSE	ADM	ADS
EBE	0.00998±0.00039	0.04182±0.00346	0.02366±0.00224	0.02073±0.00483
SSEBE	0.00842±0.00030	0.03375±0.00191	0.03695±0.00104	0.01678±0.00125
SCEE	0.01075±0.00000	0.05792±0.00000	0.03960±0.00000	0.02383±0.00000
MOEBE	**0.00839±0.00070**	**0.01746±0.00167**	**0.00883±0.00128**	**0.00442±0.00076**

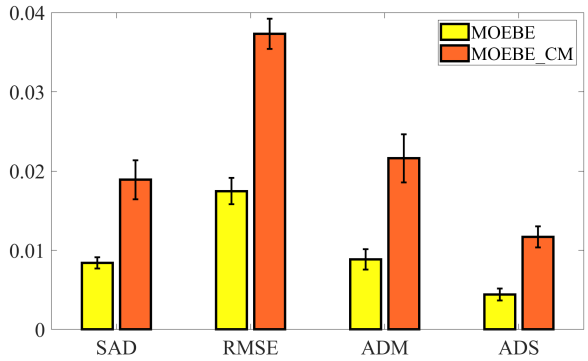

Fig. 8. Comparison results of the two velocity and position updating strategies.

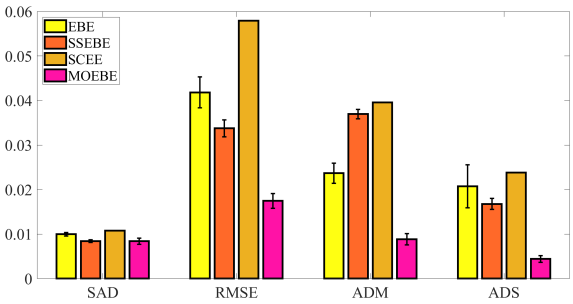

Fig. 9. Mean SAD, RMSE, ADM, and ADS of all the endmember classes from the results of synthetic data set.

deviations of the ten runs. In particular, the standard deviations for SCEE were zero, which indicated that the endmembers extracted by SCEE were the same for each run with the same parameters. The average SAD of all the endmember classes for MOEBE was slightly smaller than that for SSEBE, as well as smaller than those for EBE and SCEE. Results from MOEBE had much smaller RMSE, ADS, and ADM than those from EBE, SSEBE, and SCEE. The SAD, RMSE, ADM, and ADS were calculated for each endmember class (see Figs. 10–13, respectively). The SAD, ADM, and ADS of the sixth endmember class for SCEE were empty because SCEE failed to extract any endmembers in this class, which resulted in a large RMSE for this endmember class. Mixed pixels may have been extracted by EBE, resulting in much larger SAD of the ninth endmember class than those of other methods. The ADM and ADS for EBE, SSEBE, and SCEE had big differences among different endmember classes, whereas more balanced ADM and ADS were obtained by MOEBE. MOEBE outperformed other methods in terms of RMSE for each endmember class.

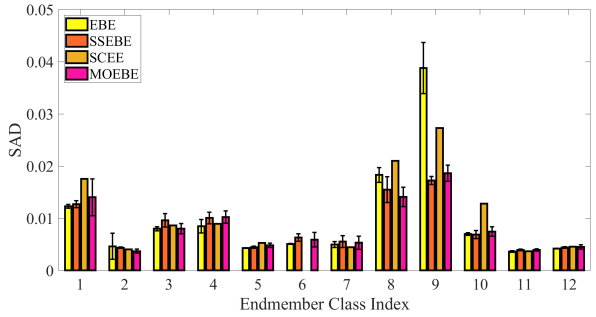

Fig. 10. SAD of each endmember class from the results of synthetic data set.

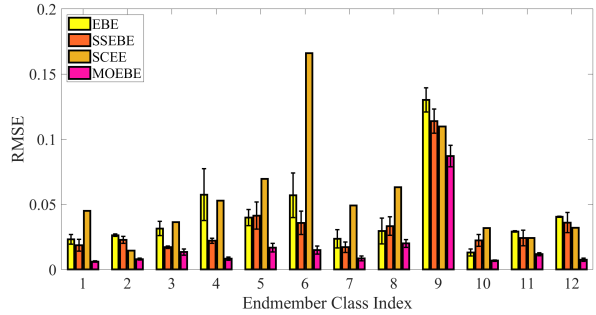

Fig. 11. RMSE of each endmember class from the results of synthetic data set.

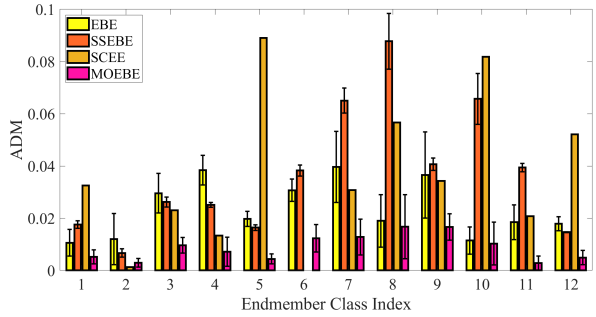

Fig. 12. ADM of each endmember class from the results of synthetic data set.

Finally, the mean and standard deviations of computational times for ten runs are shown in Table III. The 64-b version of MATLAB was implemented on a 3.4-GHz Intel Core i7. The results indicate that EBE was much cheaper computationally than other methods.

2) Results of Experiment 2 (Using the Samson Data Set): There was only a single reference endmember spectrum to be compared with the multiple endmembers within an

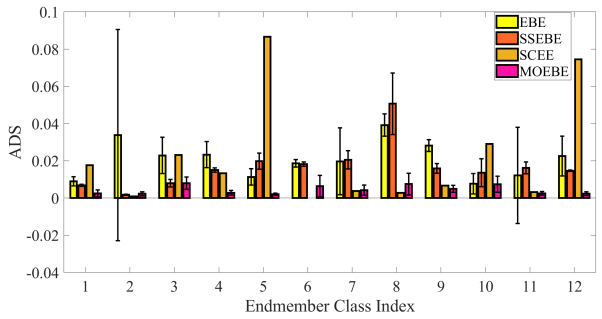

Fig. 13. ADS of each endmember class from the results of synthetic data set.

TABLE III
MEAN AND STANDARD DEVIATIONS OF COMPUTATIONAL TIMES FOR TEN RUNS

Method	EBE	SSEBE	SCEE	MOEBE
Time (Sec)	**3.51±0.12**	357.07±42.17	748.51±50.54	495.04±225.16

TABLE IV
SAD BETWEEN EXTRACTED ENDMEMBERS AND REFERENCES FOR THE SAMSON DATA SET

Material	EBE	SSEBE	SCEE	MOEBE
Soil	0.0485	0.0558	0.0466	**0.0372**
Tree	0.0637	0.0698	0.0799	**0.0394**
Water	0.1054	**0.0862**	0.0994	0.1035
Mean	0.0726	0.0706	0.0753	**0.0600**

TABLE V
RMSE BETWEEN ESTIMATED ABUNDANCES AND REFERENCES FOR THE SAMSON DATA SET

Material	EBE	SSEBE	SCEE	MOEBE
Soil	0.0813	0.0822	**0.0723**	0.0815
Tree	0.0703	0.0660	0.0624	**0.0590**
Water	0.0731	0.0806	**0.0713**	0.0829
Mean	0.0749	0.0763	**0.0687**	0.0745

endmember class for the real image experiments. Extracted endmembers within one class were compared to the same reference endmember spectrum and the mean SAD was recorded. Here a small SAD can only indicate that the extracted endmembers were not likely to be mixed pixels, but it cannot demonstrate that the multiple endmembers within each class have similar spectral variability to the true variability. Nevertheless, RMSE can reflect the accuracy of multiple endmembers, since the RMSE would be small if endmembers with variability were accurately extracted. Samson is an image with very simple ground objects, and all methods achieved abundance maps similar to the reference abundance maps by using the extracted multiple endmembers (see Fig. 14). Although MOEBE had the smallest mean SAD among the four methods (see Table IV), SCEE estimated abundances more accurately than the other methods (see Table V). The overall performances of EBE, SSEBE, SCEE, and MOEBE were similar. From the results of computational times (see Table VI),

TABLE VI
COMPUTATIONAL TIMES REQUIRED FOR THE SAMSON DATA SET

Method	EBE	SSEBE	SCEE	MOEBE
Time (Sec)	**0.55**	44.50	151.39	25.77

TABLE VII
SAD BETWEEN EXTRACTED ENDMEMBERS AND REFERENCES FOR THE JASPER RIDGE DATA SET

Material	EBE	SSEBE	SCEE	MOEBE
Tree	0.1195	**0.0821**	0.1324	0.0881
Water	0.2178	0.2889	0.2579	**0.1913**
Soil	0.1166	**0.1109**	0.1194	0.1156
Road	0.0840	0.1327	0.0754	**0.0521**
Mean	0.1345	0.1536	0.1463	**0.1118**

TABLE VIII
RMSE BETWEEN ESTIMATED ABUNDANCES AND REFERENCES FOR THE JASPER RIDGE DATA SET

Material	EBE	SSEBE	SCEE	MOEBE
Tree	0.1140	0.0945	0.0972	**0.0899**
Water	0.1139	0.0961	**0.0688**	0.0852
Soil	0.1012	0.1467	0.1144	**0.1003**
Road	0.1014	0.0935	0.1053	**0.0629**
Mean	0.1076	0.1077	0.0964	**0.0846**

TABLE IX
COMPUTATIONAL TIMES REQUIRED FOR THE JASPER RIDGE DATA SET

Method	EBE	SSEBE	SCEE	MOEBE
Time (Sec)	**1.05**	64.22	173.34	220.29

EBE was the most computationally efficient method, and SCEE spent more time than other methods.

3) Results of Experiment 3 (Using the Jasper Ridge Data Set): The estimated abundance maps created by using multiple endmembers extracted by EBE, SSEBE, SCEE, and MOEBE are shown in Fig. 15. The abundance map of tree produced by EBE and soil produced by SSEBE were obviously darker than the reference maps. The abundance maps of water produced by all methods lost some detail, compared with the reference map. From the results of SAD in Table VII and RMSE in Table VIII, MOEBE produced smaller SAD and RMSE than did EBE, SSEBE, and MOEBE. From the results of computational times (see Table IX), EBE was the most computationally efficient method, and MOEBE spent the most time.

4) Results of Experiment 4 (Using the Urban Data Set): The scene in the Urban data is more complex than that of Samson and Jasper Ridge. In addition to natural ground objects, man-made objects also appear in the Urban data. The estimated abundance maps of EBE, SSEBE, SCEE, and MOEBE are shown in Fig. 16. For EBE, there were obvious differences between the produced and reference abundance maps of asphalt road and soil, and the abundance fractions of roof#2 were overestimated. For SSEBE, abundance maps

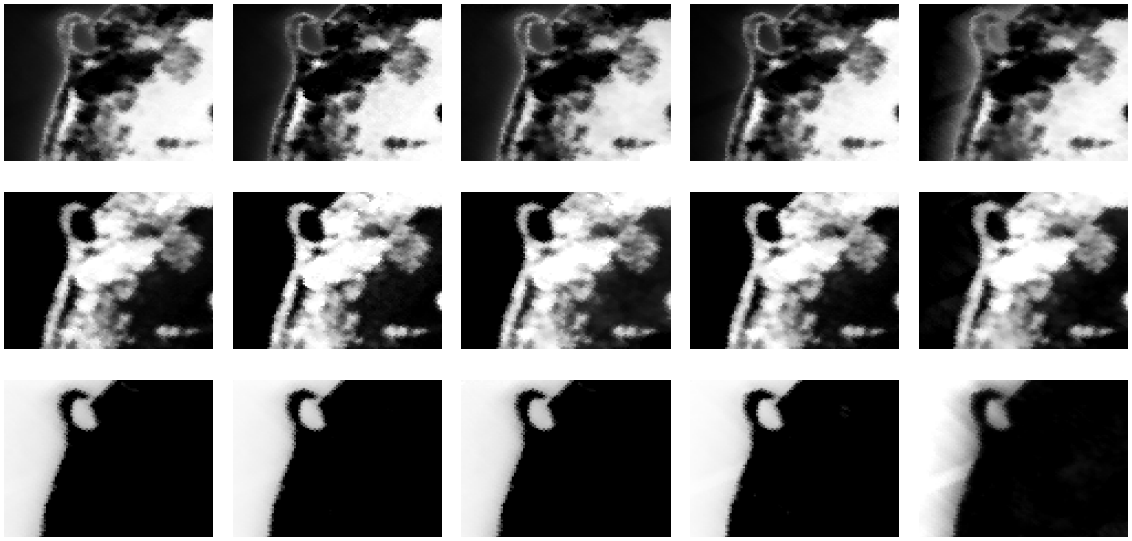

(a) EBE (b) SSEBE (c) SCEE (d) MOEBE (e) Reference

Fig. 14. Reference abundance maps and estimated abundance maps created by using multiple endmembers extracted by EBE, SSEBE, SCEE, and MOEBE for the Samson data set. The endmember classes from top to bottom are: soil, tree and water. (a) EBE. (b) SSEBE. (c) SCEE. (d) MOEBE. (e) Reference.

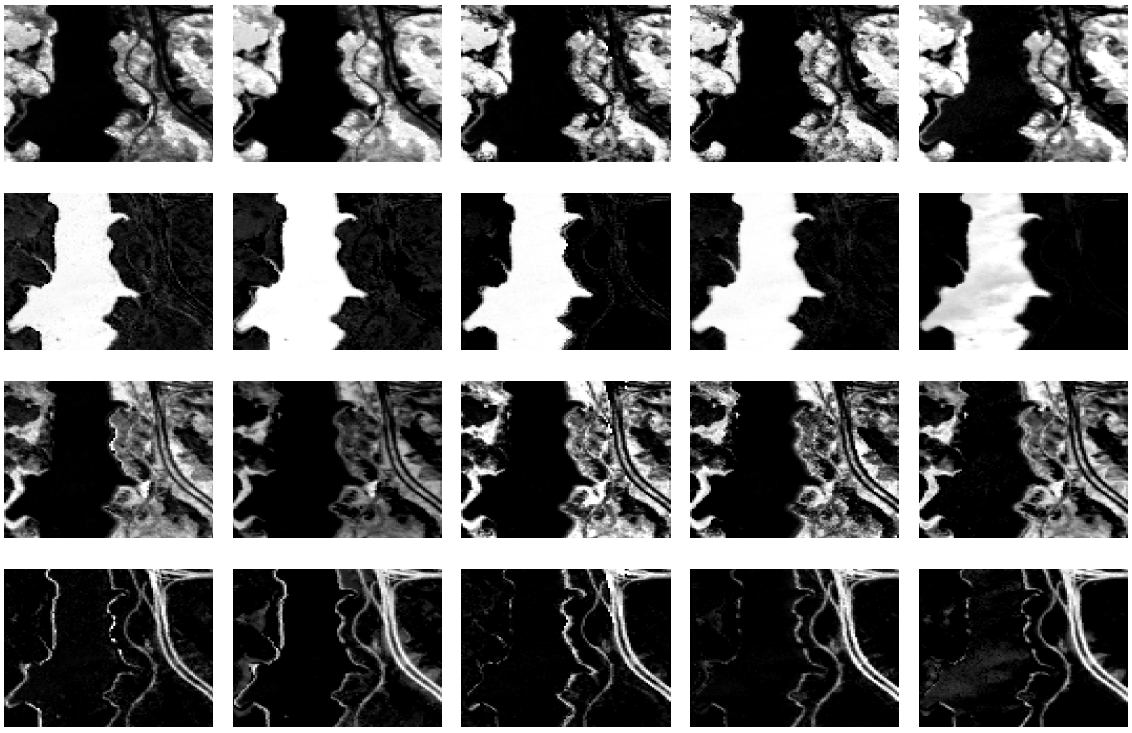

(a) EBE (b) SSEBE (c) SCEE (d) MOEBE (e) Reference

Fig. 15. Reference abundance maps and estimated abundance maps created by using multiple endmembers extracted by EBE, SSEBE, SCEE, and MOEBE for the Jasper Ridge data set. The endmember classes from top to bottom are: tree, water, soil and road. (a) EBE. (b) SSEBE. (c) SCEE. (d) MOEBE. (e) Reference.

of asphalt road, roof#2, and soil were obviously different from those of the reference maps, where the abundance fractions of roof#2 were underestimated for some pixels, and the abundance fractions of asphalt road and soil were overestimated. For SCEE, the abundance map of soil was partly different from that of the reference abundance map, and the map of grass was darker than that of the reference map. For MOEBE, the abundance fractions of tree were overestimated for some pixels. The overall performance of MOEBE was the best visually. SSEBE had the smallest SAD and MOEBE had the smallest RMSE among all the methods (see Tables X and XI). The SAD and RMSE for SSEBE and MOEBE were much

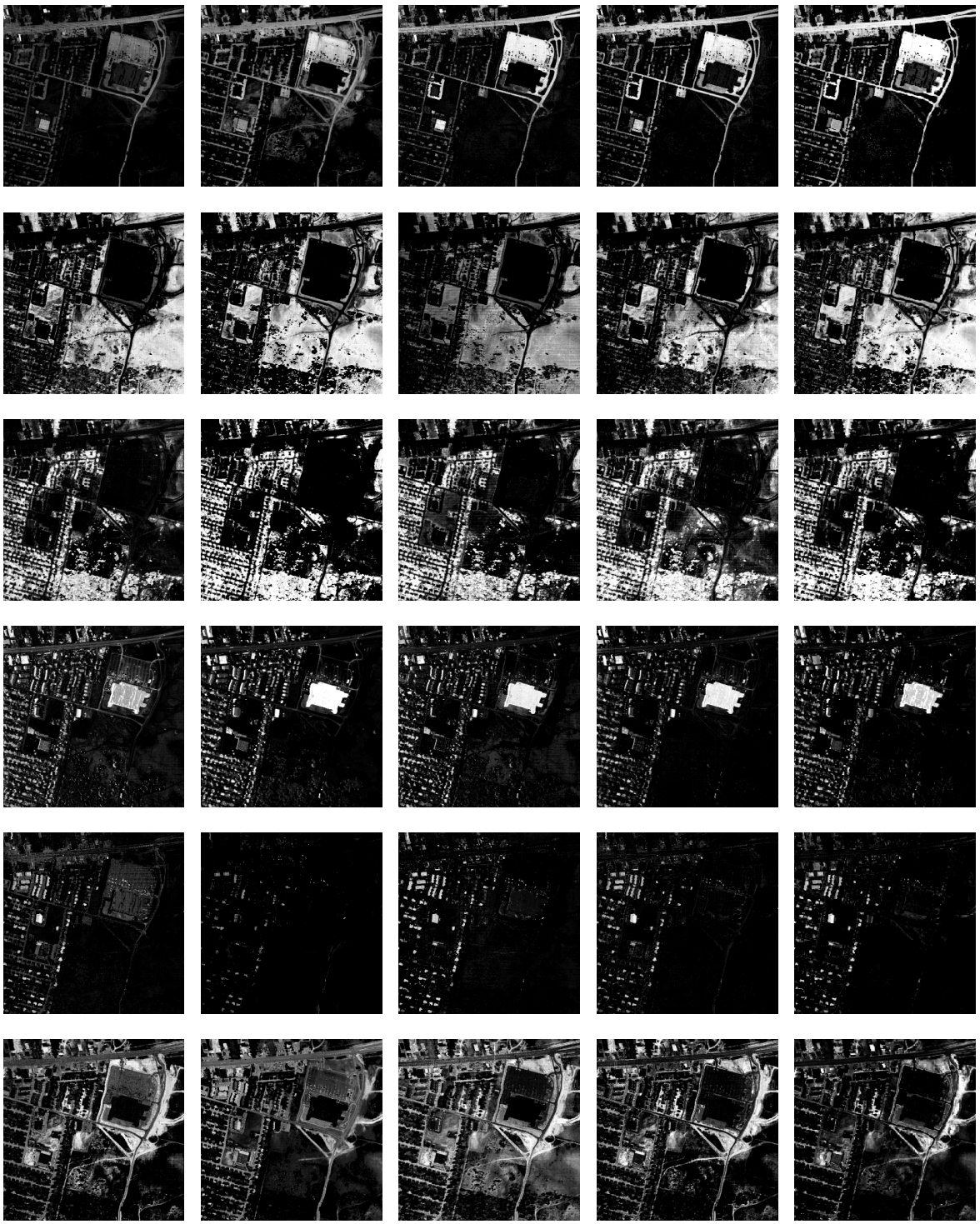

(a) EBE (b) SSEBE (c) SCEE (d) MOEBE (e) Reference

Fig. 16. Reference abundance maps and estimated abundance maps created by using multiple endmembers extracted by EBE, SSEBE, SCEE, and MOEBE for the Urban data. The endmember classes from top to bottom are: asphalt road, grass, tree, roof#1, roof#2 and soil. (a) EBE. (b) SSEBE. (c) SCEE. (d) MOEBE. (e) Reference.

smaller than those of EBE and SCEE. From the results of computational times shown in Table XII, EBE was the most computationally efficient method.

E. Discussion

The results of the four experiments indicate that EBE, SSEBE, SCEE, and MOEBE performed well for the two relatively simple images in Samson and Jasper Ridge, in which only endmembers of natural materials were to be extracted and the number of endmember classes was small. When these four methods were applied to extract multiple endmembers for the synthetic and Urban images, some of the results were not satisfactory. Although the synthetic image has only a simple type of noise (no noise or error from the imaging process

TABLE X
SAD BETWEEN EXTRACTED ENDMEMBERS AND REFERENCES FOR THE URBAN DATA SET

Material	EBE	SSEBE	SCEE	MOEBE
Asphalt Road	0.1820	0.1700	0.1520	**0.1436**
Grass	0.1328	**0.0662**	0.1889	0.1489
Tree	0.1244	**0.0790**	0.2047	0.1204
Roof#1	0.3151	0.1412	0.2569	**0.1277**
Roof#2	0.1802	0.2327	0.2015	**0.1460**
Soil	0.1232	0.1066	**0.1036**	0.1114
Mean	0.1763	**0.1326**	0.1846	0.1330

TABLE XI
RMSE BETWEEN ESTIMATED ABUNDANCES AND REFERENCES FOR THE URBAN DATA SET

Material	EBE	SSEBE	SCEE	MOEBE
Asphalt Road	0.2186	0.1745	0.1415	**0.0946**
Grass	0.1704	**0.0991**	0.2260	0.1631
Tree	0.1205	**0.0900**	0.1069	0.1278
Roof#1	0.1090	**0.0650**	0.0802	0.0684
Roof#2	0.0932	0.0946	0.0637	**0.0508**
Soil	0.1514	0.1786	0.1920	**0.1210**
Mean	0.1439	0.1170	0.1351	**0.1043**

TABLE XII
COMPUTATIONAL TIMES REQUIRED FOR THE URBAN DATA SET

Method	EBE	SSEBE	SCEE	MOEBE
Time (Sec)	**3.77**	618.81	963.34	380.68

and no anomaly) compared with the real images, it contains 12 classes of endmembers with 11 kinds of minerals and the vegetation class, which increases the complexity of the image. In this experiment, some extracted endmembers from EBE had a large SAD from the reference endmembers. This showed that mixed pixels may have been extracted as endmembers by EBE. EBE extracts endmembers from randomly selected subsets, so the mixed pixels could be mistakenly extracted as endmembers once the endmember of one class is absent in the subset. The ADM and ADS of some endmember classes were large for SSEBE, which indicated that some endmembers within the endmember class may have been lost by SSEBE. SCEE failed to extract one class of endmembers. Because SCEE utilizes the connected region to remove mixed pixels from candidate endmembers, true endmembers may also be removed if they are not located in the connected region. This is not good for the identification of rare endmembers. MOEBE performed well in extracting multiple endmembers for each of the endmember classes, and the variability of spectra within each class was close to the true variability. This is an indicator of MOEBE's potential. The Urban image has only six endmember classes, but it is affected by various noises or interferences and contains both natural and man-made materials, which result in a complex scene. EBE and SSEBE performed poorly in this experiment, which implies that the multiple spectra extracted by these two methods were not able to represent true endmember variability well for this image. EBE may have introduced mixed pixels in the endmember set. SSEBE failed to extract the endmembers located within the boundary of data simplex, leading to inaccurate variability within the endmember class. SCEE and MOEBE were able to provide multiple endmembers describing the variability within the endmember class more accurately.

EBE had very high efficiency in computational time for the four experiments. For SSEBE and SCEE, the computational time increased as the image size increased. The PPI method used in SSEBE conducts a large number of random projections for the pixels, so it will take more time to do the projections if the number of pixels increases. Since one step of SCEE applies the wavelet transform to the input image with several different scale factors, an image of a larger size will cost more time. In MOEBE, it only takes tens of seconds to get the candidate endmembers and the image size has little effect on the time cost. The most time-consuming part for MOEBE is the mixed pixel removal by SFFS. It will spend more time to get the result if the number of extracted endmembers increases.

V. CONCLUSION

A novel method, MOEBE, which extracts multiple endmembers with variability within endmember classes has been demonstrated. MOEBE constructs subspaces of the original image, and simultaneously searches endmembers in multiple spaces by using multiobjective particle swarm optimization. The comparison of MOEBE with EBE, SSEBE, and SCEE using synthetic data showed that MOEBE obtained more accurate results than did the other methods. Multiple endmember spectra obtained by MOEBE represented the true variability well for each endmember class. The abundance maps generated with multiple endmembers extracted by MOEBE were reliable under the complex scene of a real image.

REFERENCES

[1] N. Yokoya, J. C.-W. Chan, and K. Segl, "Potential of resolution-enhanced hyperspectral data for mineral mapping using simulated EnMAP and Sentinel-2 images," *Remote Sens.*, vol. 8, no. 3, p. 172, 2016.
[2] T. A. Carrino, A. P. Crósta, C. L. B. Toledo, and A. M. Silva, "Hyperspectral remote sensing applied to mineral exploration in Southern Peru: A multiple data integration approach in the Chapi Chiara gold prospect," *Int. J. Appl. Earth Observ. Geoinf.*, vol. 64, pp. 287–300, Feb. 2018.
[3] L. He *et al.*, "Improved remote sensing of leaf nitrogen concentration in winter wheat using multi-angular hyperspectral data," *Remote Sens. Environ.*, vol. 174, pp. 122–133, Mar. 2016.
[4] A. Ibrahim *et al.*, "Atmospheric correction for hyperspectral ocean color retrieval with application to the hyperspectral imager for the coastal ocean (HICO)," *Remote Sens. Environ.*, vol. 204, pp. 60–75, Jan. 2018.
[5] S. Veraverbeke *et al.*, "Hyperspectral remote sensing of fire: State-of-the-art and future perspectives," *Remote Sens. Environ.*, vol. 216, pp. 105–121, Oct. 2018.
[6] B. Du, L. Ru, C. Wu, and L. Zhang, "Unsupervised deep slow feature analysis for change detection in multi-temporal remote sensing images," *IEEE Trans. Geosci. Remote Sens.*, vol. 57, no. 12, pp. 9976–9992, Dec. 2019.
[7] J. W. Boardman, "Automating spectral unmixing of aviris data using convex geometry concepts," in *Proc. Summaries 4th Annu. JPL Airborne Geosci. Workshop*, 1993, pp. 11–14.
[8] M. E. Winter, "N-FINDR: An algorithm for fast autonomous spectral end-member determination in hyperspectral data," in *Proc. Imag. Spectrometry V*, vol. 3753, Oct. 1999, pp. 266–275.

[9] J. M. P. Nascimento and J. M. B. Dias, "Vertex component analysis: A fast algorithm to unmix hyperspectral data," *IEEE Trans. Geosci. Remote Sens.*, vol. 43, no. 4, pp. 898–910, Apr. 2005.

[10] C.-I. Chang, C.-C. Wu, W. Liu, and Y.-C. Ouyang, "A new growing method for simplex-based endmember extraction algorithm," *IEEE Trans. Geosci. Remote Sens.*, vol. 44, no. 10, pp. 2804–2819, Oct. 2006.

[11] A. Plaza, P. Martinez, R. Perez, and J. Plaza, "A quantitative and comparative analysis of endmember extraction algorithms from hyperspectral data," *IEEE Trans. Geosci. Remote Sens.*, vol. 42, no. 3, pp. 650–663, Mar. 2004.

[12] T.-H. Chan, W.-K. Ma, A. Ambikapathi, and C.-Y. Chi, "A simplex volume maximization framework for hyperspectral endmember extraction," *IEEE Trans. Geosci. Remote Sens.*, vol. 49, no. 11, pp. 4177–4193, Nov. 2011.

[13] E. M. T. Hendrix, I. Garcia, J. Plaza, G. Martin, and A. Plaza, "A new minimum-volume enclosing algorithm for endmember identification and abundance estimation in hyperspectral data," *IEEE Trans. Geosci. Remote Sens.*, vol. 50, no. 7, pp. 2744–2757, Jul. 2012.

[14] L. Miao and H. Qi, "Endmember extraction from highly mixed data using minimum volume constrained nonnegative matrix factorization," *IEEE Trans. Geosci. Remote Sens.*, vol. 45, no. 3, pp. 765–777, Mar. 2007.

[15] S. Zhang, A. Agathos, and J. Li, "Robust minimum volume simplex analysis for hyperspectral unmixing," *IEEE Trans. Geosci. Remote Sens.*, vol. 55, no. 11, pp. 6431–6439, Nov. 2017.

[16] X. Lu, L. Dong, and Y. Yuan, "Subspace clustering constrained sparse NMF for hyperspectral unmixing," *IEEE Trans. Geosci. Remote Sens.*, vol. 58, no. 5, pp. 3007–3019, May 2020.

[17] X.-R. Feng, H.-C. Li, J. Li, Q. Du, A. Plaza, and W. J. Emery, "Hyperspectral unmixing using sparsity-constrained deep nonnegative matrix factorization with total variation," *IEEE Trans. Geosci. Remote Sens.*, vol. 56, no. 10, pp. 6245–6257, Oct. 2018.

[18] R. Liu, B. Du, and L. Zhang, "Hyperspectral unmixing via double abundance characteristics constraints based NMF," *Remote Sens.*, vol. 8, no. 6, p. 464, May 2016.

[19] D. Hong, N. Yokoya, J. Chanussot, and X. X. Zhu, "An augmented linear mixing model to address spectral variability for hyperspectral unmixing," *IEEE Trans. Image Process.*, vol. 28, no. 4, pp. 1923–1938, Apr. 2019.

[20] C. A. Bateson, G. P. Asner, and C. A. Wessman, "Endmember bundles: A new approach to incorporating endmember variability into spectral mixture analysis," *IEEE Trans. Geosci. Remote Sens.*, vol. 38, no. 2, pp. 1083–1094, Mar. 2000.

[21] B. Somers, G. P. Asner, L. Tits, and P. Coppin, "Endmember variability in spectral mixture analysis: A review," *Remote Sens. Environ.*, vol. 115, no. 7, pp. 1603–1616, Jul. 2011.

[22] D. A. Roberts, M. Gardner, R. Church, S. Ustin, G. Scheer, and R. O. Green, "Mapping chaparral in the santa monica mountains using multiple endmember spectral mixture models," *Remote Sens. Environ.*, vol. 65, no. 3, pp. 267–279, Sep. 1998.

[23] J. Degerickx, D. A. Roberts, and B. Somers, "Enhancing the performance of multiple endmember spectral mixture analysis (MESMA) for urban land cover mapping using airborne lidar data and band selection," *Remote Sens. Environ.*, vol. 221, pp. 260–273, Feb. 2019.

[24] K. Canham, A. Schlamm, A. Ziemann, B. Basener, and D. Messinger, "Spatially adaptive hyperspectral unmixing," *IEEE Trans. Geosci. Remote Sens.*, vol. 49, no. 11, pp. 4248–4262, Nov. 2011.

[25] B. Somers, M. Zortea, A. Plaza, and G. P. Asner, "Automated extraction of image-based endmember bundles for improved spectral unmixing," *IEEE J. Sel. Topics Appl. Earth Observ. Remote Sens.*, vol. 5, no. 2, pp. 396–408, Apr. 2012.

[26] M. Xu, L. Zhang, and B. Du, "An image-based endmember bundle extraction algorithm using both spatial and spectral information," *IEEE J. Sel. Topics Appl. Earth Observ. Remote Sens.*, vol. 8, no. 6, pp. 2607–2617, Jun. 2015.

[27] M. Xu, L. Zhang, B. Du, and L. Zhang, "An image-based endmember bundle extraction algorithm using reconstruction error for hyperspectral imagery," *Neurocomputing*, vol. 173, pp. 397–405, Jan. 2016.

[28] M. Xu, G. Zhang, Y. Fan, B. Du, and J. Li, "Archetypal analysis for endmember bundle extraction considering spectral variability," in *Proc. 9th Workshop Hyperspectral Image Signal Process., Evol. Remote Sens. (WHISPERS)*, Sep. 2018, pp. 1–4.

[29] Z. Hua, X. Li, and L. Zhao, "Endmember bundle extraction based on pure pixel index and superpixel segmentation," in *Proc. IEEE Int. Geosci. Remote Sens. Symp. (IGARSS)*, Jul. 2019, pp. 2131–2134.

[30] T. Uezato, R. J. Murphy, A. Melkumyan, and A. Chlingaryan, "A novel endmember bundle extraction and clustering approach for capturing spectral variability within endmember classes," *IEEE Trans. Geosci. Remote Sens.*, vol. 54, no. 11, pp. 6712–6731, Nov. 2016.

[31] B. Zhang, X. Sun, L. Gao, and L. Yang, "Endmember extraction of hyperspectral remote sensing images based on the discrete particle swarm optimization algorithm," *IEEE Trans. Geosci. Remote Sens.*, vol. 49, no. 11, pp. 4173–4176, Nov. 2011.

[32] C. Zhang, Q. Qin, T. Zhang, Y. Sun, and C. Chen, "Endmember extraction from hyperspectral image based on discrete firefly algorithm (EE-DFA)," *ISPRS J. Photogramm. Remote Sens.*, vol. 126, pp. 108–119, Apr. 2017.

[33] Y. Zhong, L. Zhao, and L. Zhang, "An adaptive differential evolution endmember extraction algorithm for hyperspectral remote sensing imagery," *IEEE Geosci. Remote Sens. Lett.*, vol. 11, no. 6, pp. 1061–1065, Jun. 2014.

[34] X. Sun, L. Yang, B. Zhang, L. Gao, and J. Gao, "An endmember extraction method based on artificial bee colony algorithms for hyperspectral remote sensing images," *Remote Sens.*, vol. 7, no. 12, pp. 16363–16383, Dec. 2015.

[35] R. Liu, L. Zhang, and B. Du, "A novel endmember extraction method for hyperspectral imagery based on quantum-behaved particle swarm optimization," *IEEE J. Sel. Topics Appl. Earth Observ. Remote Sens.*, vol. 10, no. 4, pp. 1610–1631, Apr. 2017.

[36] B. Zhang, X. Sun, L. Gao, and L. Yang, "Endmember extraction of hyperspectral remote sensing images based on the ant colony optimization (ACO) algorithm," *IEEE Trans. Geosci. Remote Sens.*, vol. 49, no. 7, pp. 2635–2646, Jul. 2011.

[37] B. Du, Q. Wei, and R. Liu, "An improved quantum-behaved particle swarm optimization for endmember extraction," *IEEE Trans. Geosci. Remote Sens.*, vol. 57, no. 8, pp. 6003–6017, Aug. 2019.

[38] R. Liu, B. Du, and L. Zhang, "Multiobjective optimized endmember extraction for hyperspectral image," *Remote Sens.*, vol. 9, no. 6, p. 558, Jun. 2017.

[39] Q. Cheng, B. Du, L. Zhang, and R. Liu, "ANSGA-III: A multiobjective endmember extraction algorithm for hyperspectral images," *IEEE J. Sel. Topics Appl. Earth Observ. Remote Sens.*, vol. 12, no. 2, pp. 700–721, Feb. 2019.

[40] L. Tong, B. Du, R. Liu, and L. Zhang, "An improved multiobjective discrete particle swarm optimization for hyperspectral endmember extraction," *IEEE Trans. Geosci. Remote Sens.*, vol. 57, no. 10, pp. 7872–7882, Oct. 2019.

[41] X. Zhang, X. Zheng, R. Cheng, J. Qiu, and Y. Jin, "A competitive mechanism based multi-objective particle swarm optimizer with fast convergence," *Inf. Sci.*, vol. 427, pp. 63–76, Feb. 2018.

[42] L. Sun, Y. Zhang, and B. Guindon, "Improved iterative error analysis for endmember extraction from hyperspectral imagery," in *Proc. 13th Imag. Spectrometry*, Aug. 2008, p. 70860.

[43] N. Keshava and J. F. Mustard, "Spectral unmixing," *IEEE Signal Process. Mag.*, vol. 19, no. 1, pp. 44–57, Jan. 2002.

[44] A. H. F. Dias and J. A. de Vasconcelos, "Multiobjective genetic algorithms applied to solve optimization problems," *IEEE Trans. Magn.*, vol. 38, no. 2, pp. 1133–1136, Mar. 2002.

[45] D. Gong, J. Sun, and Z. Miao, "A set-based genetic algorithm for interval many-objective optimization problems," *IEEE Trans. Evol. Comput.*, vol. 22, no. 1, pp. 47–60, Feb. 2018.

[46] G. Bello-Orgaz, S. Salcedo-Sanz, and D. Camacho, "A multi-objective genetic algorithm for overlapping community detection based on edge encoding," *Inf. Sci.*, vol. 462, pp. 290–314, Sep. 2018.

[47] H. Li and Q. Zhang, "Multiobjective optimization problems with complicated Pareto sets, MOEA/D and NSGA-II," *IEEE Trans. Evol. Comput.*, vol. 13, no. 2, pp. 284–302, Apr. 2009.

[48] A. Jamali, R. Mallipeddi, M. Salehpour, and A. Bagheri, "Multi-objective differential evolution algorithm with fuzzy inference-based adaptive mutation factor for Pareto optimum design of suspension system," *Swarm Evol. Comput.*, vol. 54, May 2020, Art. no. 100666.

[49] Y. Tian, X. Zheng, X. Zhang, and Y. Jin, "Efficient large-scale multi-objective optimization based on a competitive swarm optimizer," *IEEE Trans. Cybern.*, vol. 50, no. 8, pp. 3696–3708, Aug. 2020.

[50] J. Tian, Y. Tan, J. Zeng, C. Sun, and Y. Jin, "Multiobjective infill criterion driven Gaussian process-assisted particle swarm optimization of high-dimensional expensive problems," *IEEE Trans. Evol. Comput.*, vol. 23, no. 3, pp. 459–472, Jun. 2019.

[51] D. Liu, K. C. Tan, C. K. Goh, and W. K. Ho, "A multiobjective memetic algorithm based on particle swarm optimization," *IEEE Trans. Syst., Man, Cybern. B, Cybern.*, vol. 37, no. 1, pp. 42–50, Feb. 2007.

[52] M. Abedi, R. Chiong, N. Noman, and R. Zhang, "A multi-population, multi-objective memetic algorithm for energy-efficient job-shop scheduling with deteriorating machines," *Expert Syst. Appl.*, vol. 157, Nov. 2020, Art. no. 113348.
[53] L. Ke, Q. Zhang, and R. Battiti, "MOEA/D-ACO: A multiobjective evolutionary algorithm using decomposition and AntColony," *IEEE Trans. Cybern.*, vol. 43, no. 6, pp. 1845–1859, Dec. 2013.
[54] Q. Zhang and H. Li, "MOEA/D: A multiobjective evolutionary algorithm based on decomposition," *IEEE Trans. Evol. Comput.*, vol. 11, no. 6, pp. 712–731, Dec. 2007.
[55] Y. Yuan, H. Xu, B. Wang, B. Zhang, and X. Yao, "Balancing convergence and diversity in decomposition-based many-objective optimizers," *IEEE Trans. Evol. Comput.*, vol. 20, no. 2, pp. 180–198, Apr. 2016.
[56] D. Han, W. Du, W. Du, Y. Jin, and C. Wu, "An adaptive decomposition-based evolutionary algorithm for many-objective optimization," *Inf. Sci.*, vol. 491, pp. 204–222, Jul. 2019.
[57] E. Zitzler and S. Künzli, "Indicator-based selection in multiobjective search," in *Proc. Int. Conf. Parallel Problem Solving Nature*. Berlin, Germany: Springer, 2004, pp. 832–842.
[58] J. Bader and E. Zitzler, "HypE: An algorithm for fast hypervolume-based many-objective optimization," *Evol. Comput.*, vol. 19, no. 1, pp. 45–76, Mar. 2011.
[59] F. Li, R. Cheng, J. Liu, and Y. Jin, "A two-stage R2 indicator based evolutionary algorithm for many-objective optimization," *Appl. Soft Comput.*, vol. 67, pp. 245–260, Jun. 2018.
[60] X. Zhang, Y. Tian, R. Cheng, and Y. Jin, "An efficient approach to nondominated sorting for evolutionary multiobjective optimization," *IEEE Trans. Evol. Comput.*, vol. 19, no. 2, pp. 201–213, Apr. 2015.
[61] G. Yu, Y. Jin, and M. Olhofer, "A multi-objective evolutionary algorithm for finding knee regions using two localized dominance relationships," *IEEE Trans. Evol. Comput.*, early access, Jul. 13, 2020, doi: 10.1109/TEVC.2020.3008877.
[62] K. Deb, A. Pratap, S. Agarwal, and T. Meyarivan, "A fast and elitist multiobjective genetic algorithm: NSGA-II," *IEEE Trans. Evol. Comput.*, vol. 6, no. 2, pp. 182–197, Apr. 2002.
[63] A. A. Green, M. Berman, P. Switzer, and M. D. Craig, "A transformation for ordering multispectral data in terms of image quality with implications for noise removal," *IEEE Trans. Geosci. Remote Sens.*, vol. 26, no. 1, pp. 65–74, Jan. 1988.
[64] K. Metaxiotis and K. Liagkouras, "A fitness guided mutation operator for improved performance of MOEAs," in *Proc. IEEE 20th Int. Conf. Electron., Circuits, Syst. (ICECS)*, Dec. 2013, pp. 751–754.
[65] D. C. Heinz, "Fully constrained least squares linear spectral mixture analysis method for material quantification in hyperspectral imagery," *IEEE Trans. Geosci. Remote Sens.*, vol. 39, no. 3, pp. 529–545, Mar. 2001.
[66] F. Zhu, Y. Wang, S. Xiang, B. Fan, and C. Pan, "Structured sparse method for hyperspectral unmixing," *ISPRS J. Photogramm. Remote Sens.*, vol. 88, pp. 101–118, Feb. 2014.
[67] F. Zhu, Y. Wang, B. Fan, S. Xiang, G. Meng, and C. Pan, "Spectral unmixing via data-guided sparsity," *IEEE Trans. Image Process.*, vol. 23, no. 12, pp. 5412–5427, Dec. 2014.
[68] F. Zhu, Y. Wang, B. Fan, G. Meng, and C. Pan, "Effective spectral unmixing via robust representation and learning-based sparsity," 2014, *arXiv:1409.0685*. [Online]. Available: http://arxiv.org/abs/1409.0685
[69] J. M. Bioucas-Dias and M. A. T. Figueiredo, "Alternating direction algorithms for constrained sparse regression: Application to hyperspectral unmixing," in *Proc. 2nd Workshop Hyperspectral Image Signal Processing: Evol. Remote Sens.*, Jun. 2010, pp. 1–4.

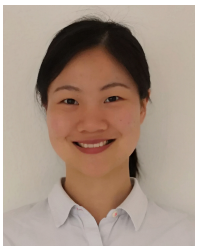

Rong Liu (Member, IEEE) received the B.S. degree in surveying and mapping engineering from Wuhan University, Wuhan, China, in 2013, and the Ph.D. degree in photogrammetry and remote sensing from the State Key Laboratory of Information Engineering in Surveying, Mapping, and Remote Sensing (LIESMARS), Wuhan University, in 2018.

She is now a Postdoctoral Researcher with German Aerospace Center (DLR), Remote Sensing Technology Institute, Weßling, Germany, and also with Signal Processing in Earth Observation, Technical University of Munich, Munich, Germany. Her research interest includes hyperspectral image processing and evolutionary computation.

Xiaoxiang Zhu (Senior Member, IEEE) received the master's (M.Sc.) degree, the doctor of engineering (Dr.-Ing.) degree, and the "Habilitation" in the field of signal processing from Technical University of Munich (TUM), Munich, Germany, in 2008, 2011, and 2013, respectively.

She is currently the Professor for Data Science in Earth Observation (former: Signal Processing in Earth Observation) at Technical University of Munich (TUM) and the Head of the Department "EO Data Science" at the Remote Sensing Technology Institute, German Aerospace Center (DLR). Since 2019, she is a co-coordinator of the Munich Data Science Research School (www.mu-ds.de). Since 2019, she also heads the Helmholtz Artificial Intelligence Cooperation Unit (HAICU)—Research Field "Aeronautics, Space and Transport." Since May 2020, she is the Director of the international future artificial intelligence (AI) lab "AI4EO—Artificial Intelligence for Earth Observation: Reasoning, Uncertainties, Ethics and Beyond," Munich, Germany. Since October 2020, she also serves in the Board of Directors of the Munich Data Science Institute (MDSI), TUM. She was a Guest Scientist or Visiting Professor at the Italian National Research Council [CNR-Institute for Electromagnetic Sensing of the Environment (IREA)], Naples, Italy, Fudan University, Shanghai, China, the University of Tokyo, Tokyo, Japan, and University of California, Los Angeles, CA, USA, in 2009, 2014, 2015, and 2016, respectively. Her main research interests are remote sensing and earth observation (EO), signal processing, machine learning and data science, with a special application focus on global urban mapping.

Dr. Zhu is a member of young academy (Junge Akademie/Junges Kolleg) at the Berlin-Brandenburg Academy of Sciences and Humanities and the German National Academy of Sciences Leopoldina, and the Bavarian Academy of Sciences and Humanities. She is an Associate Editor of IEEE TRANSACTIONS ON GEOSCIENCE AND REMOTE SENSING.